

Writing Into Water

Nadir Möller, Lukas Hecht, Ran Niu, Benno Liebchen,* and Thomas Palberg*

Writing is an ancient communication technique dating back at least 30 000 years. While even sophisticated contemporary writing techniques hinge on solid surfaces for engraving or the deposition of ink, writing within a liquid medium requires a fundamentally different approach. The study here demonstrates the writing of lines, letters, and complex patterns in water by assembling lines of colloidal particles. Unlike established techniques for underwater writing on solid substrates, these lines are fully reconfigurable and do not require any fixation onto the substrate. Exploiting gravity, an ion-exchange bead (pen) is rolled across a layer of sedimented colloidal particles (ink). The pen evokes a hydrodynamic flow collecting ink-particles into a durable, high-contrast line along its trajectory. Deliberate substrate-tilting sequences facilitate pen-steering and thus drawing and writing. The experiments are complemented with a minimal model that quantitatively predicts the observed parameter dependence for writing in fluids and highlights the generic character of writing by line-assembly. Overall, the approach opens a versatile route for writing, drawing, and patterning fluids—even at the micro-scale.

date back some 30 000 years, possibly even much longer.^[1] As a visible language, writing appeared in the Middle East between 3400 and 2600 before the Common Era.^[2,3] These techniques continue to coexist as means of storing and transporting information, nowadays accompanied by various multimedia techniques for displaying.^[4] In addition, various novel techniques extend and complement these traditional techniques, including (electron) lithography, optical tweezing, direct printing, or force microscopic manipulation.^[5–12] Remarkably, the size of glyphs and letters covers the range from a few hundred meters^[13] down to the atomic scale^[14] and even below.^[15] In the more classical approaches, one creates a local, line-shaped variation of the material density in or on an extended substrate acting as background: A line is carved out or some ink is deposited. A solid substrate stabilizes the density variation by strong intermolecular forces, keeping it in shape. The same principle has been


1. Introduction

Traditional writing techniques comprise carving and engraving as well as printing and writing with ink. Earliest human drawings

applied to write on surfaces submerged in a fluid. For instance, scanning probe lithography was used to carve or deposit lines within or onto self-assembled monolayers submerged in fluids containing suitable chemicals.^[16,17] In addition, sophisticated micron-sized structures have been printed using two-photon polymerization.^[18,19] UV-polymerization and crosslinking were also used to write on a solid surface within a liquid starting from a dispersion of reactive chemicals to manufacture patterns with superb thermoresponsive mechanical properties.^[20] There are now even commercial scuba diver slates available for underwater writing on a substrate. Importantly, however, all these approaches still rely on a substrate i) for fixing the written structures and ii) for providing mechanical support. In contrast, “writing into a fluid” requires a mechanism that does not depend on such localization measures. The mechanism must also be intrinsically robust against rapid line dispersion, which would cause short lifetimes of any drawn lines. In fact, even in a quiescent (convection-free) fluid, the moving pen would transfer kinetic energy to the fluid, provoking line dispersion by locally created eddies. While such local eddies are rather unimportant when the pen is much smaller than the written letters, as, e.g., in skywriting,^[21] the creation of fine, durable, and freely-floating lines remains challenging. In fact, to write fully reconfigurable lines into a liquid at the microscale, an approach fundamentally different from underwater ink deposition or line carving and a new type of micro-pen are required. To develop such an approach, we exploit the following ideas.

N. Möller, R. Niu^[†], T. Palberg
Institut für Physik
Johannes Gutenberg Universität
Staudinger Weg 7, 55128 Mainz, Germany
E-mail: palberg@uni-mainz.de

L. Hecht, B. Liebchen
Institute for Condensed Matter Physics
Department of Physics
Technische Universität Darmstadt
Hochschulstr. 8, 64289 Darmstadt, Germany
E-mail: benno.liebchen@pkm.tu-darmstadt.de

 The ORCID identification number(s) for the author(s) of this article can be found under <https://doi.org/10.1002/smll.202303741>

^[†]Present address: Huazhong University of Science and Technology, Luoyu Road 1037, Wuhan 430074, China

© 2023 The Authors. Small published by Wiley-VCH GmbH. This is an open access article under the terms of the Creative Commons Attribution-NonCommercial-NoDerivs License, which permits use and distribution in any medium, provided the original work is properly cited, the use is non-commercial and no modifications or adaptations are made.

DOI: 10.1002/smll.202303741

Incidentally, a mobile fluid offers an alternative way of writing lines by particle transport toward a prescribed pattern. Imagine to start from a homogenous density of ink particles in a quiescent fluid and to use a pen that attracts the ink particles toward itself and/or its trajectory. If the resulting accretion process is sufficiently efficient and fast as compared to the subsequent dispersion of the ink particles, an increase in ink density may result past the pen, and a line is written. As key ingredients, this approach requires a sufficient range of particle-transporting attraction, a slow line dispersion, and a suitable way of pen-steering.

To meet the first requirement, the directed transport of colloidal particles by chemical, thermal, or light-intensity gradients can be exploited. A key example is phoretic effects, where, in general, the imposed gradient leads to a difference in chemical potential along a particle surface and drives a slip flow of the adjacent fluid along the surface, which, in turn, evokes directed motion of the particle.^[22–26] Using a large chemical-loaded “beacon” falling under gravity, Banerjee et al. created a colloidal overdensity evolving along the trajectory within a few minutes.^[27] Here, colloidal motion relied on the local strength and direction of the gradient of electrolyte concentration. While these pioneering experiments demonstrate the possibility of writing freely buoyant lines within a fluid, they lack the option of deliberate pen steering.

In this work, we demonstrate a generic method for writing lines and letterings into a liquid rather than onto a solid. This method uses an ion-exchange resin bead (IEX) as a fully steerable micro-pen and exploits the presence of a solid substrate only for line assembly but not for fixing the ink. Instead, lines are written near a substrate but are not attached to it yielding freely floating long-lived lines which can be reconfigured and allow us to recycle the ink for writing new lines before optionally fixing them to the substrate.^[20,28,29] To achieve this, we exploit an effective way to transport colloids along extended surfaces: The ion-exchange resin bead (pen) evokes a so-called diffusio-osmotic (DO) flow.^[22,30,31] Such a flow emerges because the ion-exchange process induces a nonuniform concentration profile that causes a stress (force) on the solvent within the interfacial layer of the substrate resulting in a solvent flow towards the IEX.^[32] This flow then advects colloidal tracers towards the IEX, which can be viewed as an effective attraction between the IEX and the tracers.^[33] In the past, DO flows have been successfully employed with fixed sources,^[32–38] self-propelling sources,^[39,40] and combinations of sources and sinks^[41] to create centrally symmetric or asymmetric assemblies of tracer particles at the source. Here, we exploit this mechanism to dynamically assemble a line of tracer particles (ink) in the wake of a moving ion-exchange resin bead. Once assembled, those tracers will disperse only very slowly by thermal diffusion in the eddy-free fluid. Moreover, the ongoing pen-induced DO flows focus ink particles toward the center of the written lines supporting their durability and sharpness.

Our results exemplify a generic pathway for writing and drawing fine, free-floating but durable lines in a liquid medium. Our approach is modular and allows combinations of different inks, drives, steering, and, optionally, fixation techniques. This could be used in the future for structuring liquids with deliberate line-based patterns, decorate, and thus visualize chemical tracers, or create desired initial states for future colloid experiments.

2. Results

2.1. Writing of Straight Lines

Our experimental approach is sketched in **Figure 1a**. Samples are placed on a programmable, motorized stage, allowing for tilting by ϑ and rotation around the optical axis (OA) by φ , and are observed at moderate magnification (10× or 20×) using an inverted microscope. A dilute suspension of weakly charged, micro-sized silica spheres (Si832, tracers, T), is left to settle under gravity in a slit cell of 500 μm height onto a charged glass substrate. To this dilute homogeneous monolayer, we add a larger bead of cationic ion-exchange resin (C-IEX45, IEX). It exchanges residual cations ($c \approx 10^{-8} \text{ mol L}^{-1}$) for protons and thus acts as mobile proton source.^[32] The high proton mobility quickly establishes a large-scale pH-field.^[42] Tilting the substrate in x -direction by an angle ϑ lets this IEX roll straight across the substrate with a velocity $v_{\text{IEX}} = (gV\Delta\rho/\gamma) \sin\vartheta$ (red arrow in **Figure 1a** and **Figure S1a**, Supporting Information). Here, g is the gravitational acceleration, and V , $\Delta\rho$, and γ are the volume, density mismatch, and the drag coefficient of the IEX. Tracers also roll, but at negligibly small velocities. The rolling IEX (pen) remains embedded in its self-generated, co-moving pH-field,^[42] and the corresponding DO-flow along the substrate points towards the low pH region (green arrows). It accretes tracers towards the pen,^[22,23,39] from where they are expelled to the back leaving a trail of enhanced ink-particle density. In principle, the same mechanism could be exploited to co-assemble other small objects, e.g. initiator, (macro-)monomers, and cross-linker molecules, which could later be used to fix line centers containing high tracer density by UV curing. Note that in all figures regarding experiments, the substrate is tilted such that IEX and tracers move from right to left.

Samples are studied either in dark field (**Figure 1b**, see also **Figure S1b-d**, Supporting Information) or bright field (**Figure 1c** and **Movie S1**, Supporting Information). In the stationary state depicted in **Figure 1c**, the line drawn at $v_{\text{IEX}} = 7.7 \mu\text{m s}^{-1}$ first narrows and then broadens again. We identify a line focus (red arrow) separating an initial formation zone of length $l_f = v_{\text{IEX}} t_f$ (where $t_f \approx 60\text{--}70 \text{ s}$ denotes the time elapsing between the passage of the IEX and the line focus) from a subsequent decay zone. To quantify the underlying mechanisms, we show the co-moving, height averaged pH-field recorded in bright field using 3-channel photometry in **Figure 1d**.^[42,43] The arrows denote the local pH-gradient directions. We observe a stationary, elliptically distorted, and rather diffuse pH distribution. From this, we calculate the pH variation at the substrate height following Möller et al. (**Figure 1e**).^[42] Note that at this height, the gradients driving the DO-flow are much more pronounced. **Figure 1f** shows the resulting trajectories of individual tracers relative to the IEX. Tracers in the line of the IEX motion approach from the front and leave at the back. Tracers to the sides show bent trajectories as they are swept toward the IEX. We depict the instantaneous lateral solvent flow field in **Figure 1g** in lab coordinates and with color-coded flow strength. Note the striking similarity with **Figure 1e**. Solvent flows towards the IEX but moreover also towards and along the lateral pH-minimum extending in the wake of the IEX. Due to its incompressibility, the solvent has to flow upward at the IEX.^[32]

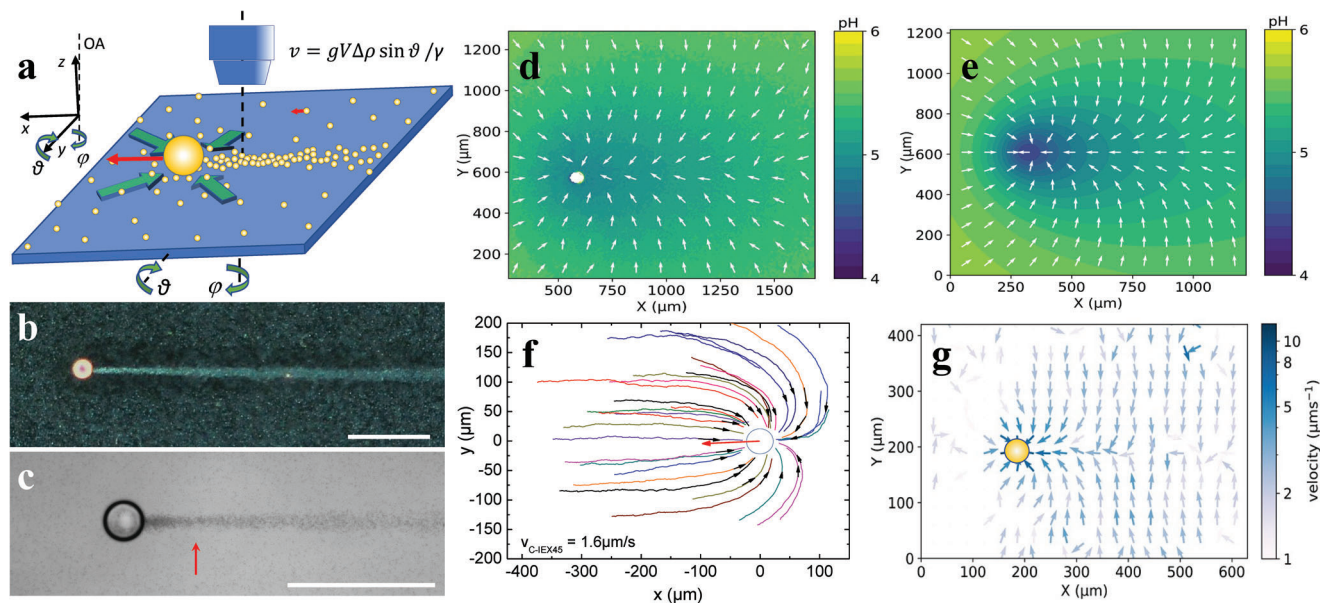


Figure 1. Writing of straight lines. a) Sketch of the experimental situation. The sample is placed on a stage allowing for tilting by θ and rotation around the optical axis (OA) by φ . The IEX (large sphere) rolls under gravity (large red arrow) through settled tracer particles (small spheres), rolling at much smaller speed (short red arrow). Tracers are swept towards the IEX by the co-moving solvent flow field (green arrows) and are assembled in the back of the IEX into a line of positive density contrast, which is left behind and disperses slowly by diffusion. b) Dark field image of C-IEX45 rolling on an inclined glass substrate ($\theta = 3.1^\circ$, substrate ζ -potential $\zeta_S = -105$ mV, $v_{\text{IEX}} = 7.7 \mu\text{m s}^{-1}$) in a suspension of Si832 at $c = 0.1$ wt.% (tracer ζ -potential $\zeta_T = -68$ mV). Scale bar: $200 \mu\text{m}$. c) The same but in bright field b/w and at $c = 0.02$ wt.%. The red arrow denotes the location of the line focus. d) Height averaged pH field in lab coordinates as determined by 3-channel micro-photometry for the experiment shown in panel (b). The pH-values are color coded as indicated in the key. Arrows denote the local gradient direction. e) Ground pH-field as derived from panel (d). f) Map of tracer approach trajectories in IEX-relative coordinates for C-IEX45 rolling at $v_{\text{IEX}} = 1.6 \mu\text{m s}^{-1}$. The red arrow denotes the rolling direction of the IEX. g) Tracer velocity field in lab coordinates as determined from Particle Image Velocimetry for the situation in panel (c). Local velocities are color coded according to the key.

To explore the influence of the IEX speed on line writing, we varied the tilt angle θ to change v_{IEX} (Figure S1b-d, Supporting Information). To good approximation, the IEX speed increases linearly with $\sin(\theta)$. For IEX speeds in the range of $1.5 \mu\text{m s}^{-1} < v_{\text{IEX}} < 11 \mu\text{m s}^{-1}$, straight single lines of long extension are obtained, with maximum contrast observed for $6 \mu\text{m s}^{-1} < v_{\text{IEX}} < 10 \mu\text{m s}^{-1}$. At lower v_{IEX} , tracers become trapped in asymmetric assemblies close to the IEX. At larger v_{IEX} , lines get rather faint and occasionally a short-lived line split is observed, with the two lines merging by diffusion.

2.2. Line Stability

For writing complex patterns, lines should be durable. The line in **Figure 2a** was written in Si832 at $c = 0.1$ wt.% for increasing times after IEX passage, which defines $t = 0$ (see also Movie S2, Supporting Information). **Figure 2b** shows the line profiles fitted by Gaussians, from which we derive the linewidth in terms of the Full Width at Half Maximum (FWHM). The FWHM increases slowly and at continually slowing pace with increasing time. Notably, even after some ten minutes, the linewidth has increased from $40 \mu\text{m}$ to merely $90 \mu\text{m}$ (**Figure 2**). The relative height of the maximum has decreased correspondingly by some 50%, and the line remains clearly visible (**Figure 2a**). We further studied the linewidth evolution for different c and v_{IEX} . The linewidth increases with tracer concentration and de-

creases with IEX speed. The double logarithmic plot of **Figure 2e** shows the time-dependent FWHM scaled to $v_{\text{IEX}} = 8 \mu\text{m s}^{-1}$ and $c = 0.1$ wt.%. Data arrange on a single straight line of slope 0.48. A systematic analysis suggests an overall scaling of the line width as $\text{FWHM} \propto v_{\text{IEX}}^{-1} c^{1/2} t^{1/2}$ (**Figure S2**, Supporting Information). This scaling is compatible with accretion at constant solvent flux and purely diffusive line dispersion.

2.3. Effective Attraction

The line formation results as the net effect of the pH-driven DO-flow and typically involves Peclet numbers of $\text{Pe} \approx 10\text{--}30$. Thus, the line formation is dominated by tracer advection caused by the DO-flow. The Reynold numbers, however, are small ($\text{Re} \approx 10^{-4}$), i.e., the flow is dominated by viscous forces and thus, laminar. Furthermore, the ratio of the tracer mass and drag coefficients is small ($m_T/\gamma_T \approx 10^{-7}$ s), and therefore, the motion of the tracers is overdamped. Overall, the DO-flow induced by the IEX leads to a directed motion of the tracers towards the moving IEX, whereas the IEX does not significantly respond to the tracers. Thus, the effective interaction between the IEX and each tracer can be described as an effective non-reciprocal attraction exerted by the IEX on the tracers leading to a center of mass motion of the tracers.^[33] We extracted the form of these effective interactions from experimentally measured velocities obtained from video-tracking (**Figure 3a**). We found that the tracer velocity field at a

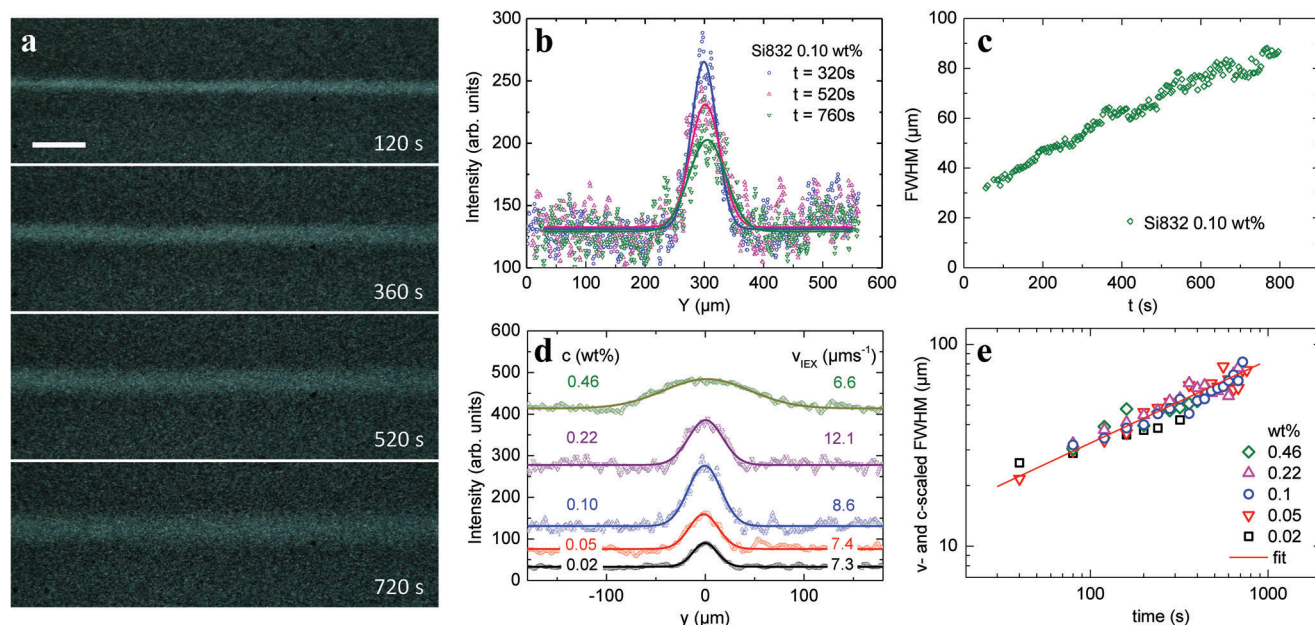


Figure 2. Line evolution past the formation zone. a) Dark field images of a line written by C-IEX45 in 0.1 wt.% Si832 for different times after IEX passage, as indicated. Scale bar: 100 μm . b) Line profiles (symbols) in lab coordinates for three selected times as indicated in the key. The solid lines are fits of Gaussians with an offset corresponding to the background scattering intensity. c) Full Width at Half Maximum (FWHM) as determined from fits to line profiles taken at different times t after IEX passage. Data are taken after the passage of the line focus. The increase in linewidth slows with time. d) Line profiles in IEX-relative coordinates obtained at different tracer concentrations and IEX speeds as indicated in the keys. These averages over 50 individual line profiles sampled over 100 μm along the lines were recorded at $t = 80$ s. All profiles are well described by fits of a Gaussian with an offset corresponding to the background scattering intensity. e) Scaling analysis: We separately determined the c -dependence and the v_{IEX} -dependence of the FWHM and scaled the obtained fit results to $c = 0.1$ wt.% and $v_{\text{IEX}} = 8 \mu\text{m s}^{-1}$. Data arrange on a straight line in this double logarithmic plot. From the fit of a linear function, we obtain $\text{FWHM} \propto t^\lambda$ with $\lambda = 0.48 \pm 0.04$, which is very close to the theoretically expected value of $\lambda = 0.5$.

distance r behind the IEX can be fitted by the following form:

$$|\vec{v}(r)| = \frac{c_1}{r^\alpha + c_2} \quad (1)$$

Thus, it yields a non-reciprocal attractive effective force of strength $F_a(r) = \gamma_T |\vec{v}(r)|$ reaching out some hundreds of microns (inset in Figure 3a and Figure S11, Supporting Information). Here, γ_T denotes the Stokes drag coefficient of the tracers. The parameters c_1 , c_2 , and α are obtained from a nonlinear least-squares fit (see Figure 3a and Supporting Information for details).

2.4. Model

Based on the effective force, we formulate a minimal (particle-based) model for the tracer dynamics at prescribed motion of the IEX. Within this model, the tracers are considered as overdamped Brownian particles, which experience a non-reciprocal effective force $\vec{F}_{\text{eff}}(t, \vec{r})$ due to the IEX as obtained from Equation (1) (see also inset of Figure 3a and Experimental Section) and are subject to thermal diffusion. The position of the i -th tracer particle evolves in time according to

$$\dot{\vec{r}}_i(t) = \frac{1}{\gamma_T} \left[\vec{F}_{\text{eff}}(t, \vec{r}_i) - \sum_{j=1, j \neq i}^N \nabla_i u(|\vec{r}_i - \vec{r}_j|) \right] + \sqrt{2D} \vec{\xi}_i(t) \quad (2)$$

where γ_T denotes the Stokes drag coefficient, $D = k_B T_{\text{bath}} / \gamma_T$ the diffusion coefficient with bath temperature T_{bath} , and $\vec{\xi}_i(t)$ denotes Gaussian white noise with zero mean and unit variance. The optionally considered (repulsive) pair interaction between the tracer particles is modeled by a Weeks-Chandler-Anderson potential $u(r)$.^[44] For simplicity, we assume that the total effective force $\vec{F}_{\text{eff}}(t, \vec{r})$ is radially symmetric (see Experimental Section for details). Clearly, this is a simplification of the overall DO-flow pattern (Figure 1g and Figure S5, Supporting Information), but, as we shall see, sufficient to capture the essentials of line writing. Motivated by the experimental observations (Figure 1), we further neglect the very slow collective tracer motion under gravity and any diffusio-phoretic motion of tracers originating from DO flows along the surfaces of the mobile tracers due to the concentration gradient.^[22] The corresponding Langevin equations for the tracer dynamics [Equation (2)] are solved numerically with a deterministically moving IEX at prescribed velocity with and without considering direct tracer-tracer interactions $u(r)$ to check the effect of the latter on the line formation (see Experimental Section and Supporting Information for details). Finally, the effective attraction leads to the formation of straight, narrow, and durable lines of increased tracer density (Figure 3b and Movie S3, Supporting Information).

To access larger length and time scales, we additionally formulate an equivalent continuum model, which is given by the two-dimensional Smoluchowski equation for the probability density $p(t, X, Y)$ of the (point-like) tracer particles [Experimental Section

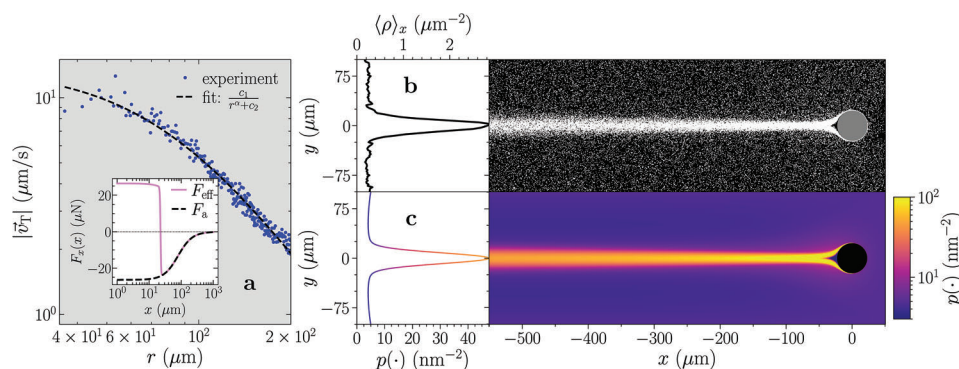


Figure 3. Modelling of line writing. a) Tracer approach speed averaged over an angular region of 30° behind the IEX rolling at $v_{\text{IEX}} = 1.6 \mu\text{m s}^{-1}$ (blue) in dependence on the radial distance r to the IEX center. The black dashed line is a nonlinear least-squares fit of Equation (1) returning $c_1 \approx (7.2 \pm 2.3) \times 10^4 \mu\text{m}^3 \text{s}^{-1}$, $c_2 \approx (5.3 \pm 1.9) \times 10^3 \mu\text{m}^2$, and $\alpha = 1.96 \pm 0.06$. Inset: x -component of effective forces as used in the continuum model. The attractive part F_a corresponds to the fit in the main panel (black dashed curve), the full effective force F_{eff} (solid pink curve) additionally accounts for volume exclusion interactions between the IEX and the tracers. b, c) Exemplary results from theoretical modeling based on the effective force shown in panel (a) in IEX-relative coordinates. Parameters were chosen to correspond closely to those of the experiments: $2a_{\text{IEX}} = 45 \mu\text{m}$, $D = 0.5 \mu\text{m}^2 \text{s}^{-1}$, $\gamma_T = 7.85 \times 10^{-9} \text{kg s}^{-1}$, $v_{\text{IEX}} = 8.0 \mu\text{m s}^{-1}$ (b) and $v_{\text{IEX}} = 8.6 \mu\text{m s}^{-1}$ (c) (see also Table 2). b) Snapshot taken at $t = 100 \text{ s}$ from a BD simulation starting from $N = 112\,200$ uniformly distributed point-like tracers. The line profile (left) is averaged over the interval $x \in [-550 \mu\text{m}, -500 \mu\text{m}]$. c) Numerical solution of Equation (6) with initially uniform probability density $p_0 = 5 \times 10^{-6} \mu\text{m}^{-2}$ after $t = 2000 \text{ s}$. The probability density $p(\cdot) = p(2000\text{s}, x, y)$ (right) and the line profile at $x = -550 \mu\text{m}$ (left) are color-coded as indicated in the key.

Equation (5)]. We solved the Smoluchowski equation numerically in the coordinate frame of the IEX [Experimental Section Equation (6)] for a deterministically moving IEX with prescribed velocity. As shown in Figure 3c, our continuum model also leads to the formation of a straight and narrow line of increased probability density.

In the continuum model, the stationary state was typically reached within a few hundred seconds (Figure S12, Supporting Information). As in our experiments, the density distribution may take different shapes in the line formation region, but beyond the focal point, the line profile is Gaussian (Figure S14, Supporting Information). Note from the profile in Figure 3c that the lines are embedded within a region of marginally reduced tracer density reflecting the extension of the accretion zone. As in the experiments, this depleted accretion region serves to enhance the contrast of the main line. Our observations demonstrate that the main ingredients of line formation are simple and generic: Writing into water requires a quick, medium-range ink-transport towards the moving pen caused by an effective hydrodynamic attraction of ink particles towards the IEX and a slow, diffusive line decay. Thus, we term this novel type of writing a line of increased density in water hydrodynamic writing (HDW).

2.5. State Diagram

Using the continuum model [based on Equation (6)], we systematically varied the IEX speed v_{IEX} (equivalent to changing the tilt angle ϑ in the experiment) and the tracer diffusion constant D (equivalent to changing the tracer particle size). To discriminate between different line types, we fitted a Gaussian or a sum of two Gaussians to the line profiles of the probability density taken in the stationary state after $t = 2000 \text{ s}$ at distance $x = -950 \mu\text{m}$ behind the IEX (Figure S15, Supporting Information). We observed

three different line types: single line, split line, and inverted line (Figure 4a). Consequently, the state diagram in the $v_{\text{IEX}}-D$ -plane shows three distinct regions (Figure 4b).

Pronounced single lines are obtained at intermediate velocities (color-coded region with state points I and II in Figure 4b). We define a line sharpness p_{max}/σ , where p_{max} denotes the amplitude of the fitted Gaussian line profile and σ denotes its standard deviation. Line sharpness, and thus, contrast, is largest at small D . With increasing diffusivity, sharpness decreases and lines get continuously broader and fainter. Towards larger velocities, the line formation length expands and results in a split line (III). The simulated profile at $x = -950 \mu\text{m}$ now shows two maxima, which eventually merge at larger distances x by diffusive broadening. The regime of split line formation is thus located in the lower right corner of the state diagram (low D , large v_{IEX}).

Interestingly, the model further reveals a third line type at low velocities. Due to the low IEX velocity, a substantial amount of attracted tracers is trapped and no line of positive density contrast is written. Instead, in the steady state, a stationary cloud of tracers forms in the vicinity of the IEX due to a balance between trapping and diffusion, which we also observed in our experiments (example IV in Figure 4c). Accretion of tracers from the IEX surroundings leads to a broad shallow minimum in the line profile, i.e., the line contrast is inverted (see example IV in Figure 4a and Figure S15a, Supporting Information). The width of the minimum mirrors the y -extension of the range of attraction. Note that such a shallow depletion zone is also present at larger IEX velocities in the single-line regime (HDW), but as in the experiments, it is masked by a much more pronounced HDW line and increases the line contrast (Figures S1c and S15b, Supporting Information).

Overall, also lines written in the model vary considerably in quality and not all appear to be useful for actual writing. In practice, all inverted lines written at low v_{IEX} remain too faint.

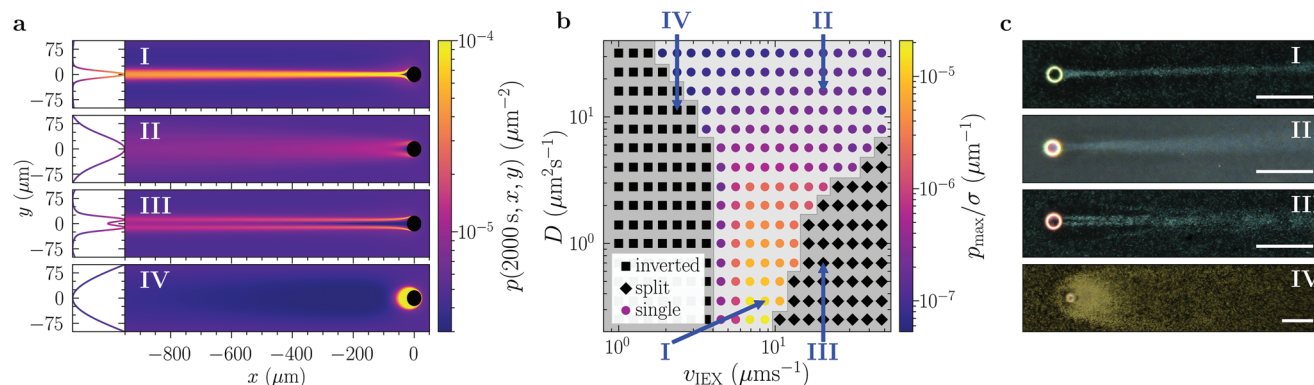


Figure 4. State diagram. a) Snapshots (right) and line profiles at $x = -950 \mu\text{m}$ (left) obtained from the numerical solution of Equation (6) in the stationary state at $t = 2000 \text{ s}$. The representative examples are denoted by Roman numerals: narrow single line (I), broad single line (II), split line (III), and inverted line (IV). Colors encode the probability density $p(2000 \text{ s}, x, y)$ as given in the key. b) State diagram in the $v_{\text{IEX}}-D$ -plane (other parameters as before, see also Experimental Section, Table 2). Symbols denote the three principal line types as discriminated by the line profiles at $x = -950 \mu\text{m}$: inverted line (squares), split line (diamonds), and single line (color-filled circles). The state points corresponding to the examples shown in panel (a) are marked by blue arrows and Roman numerals. For single lines, colors encode the line sharpness p_{max}/σ , where p_{max} denotes the amplitude of the fitted Gaussian line profile and σ denotes its standard deviation. c) Representative experimental examples observed in the three regions of the state diagram: narrow single line written in 0.10 wt.% Si832 at $v_{\text{IEX}} = 9.2 \mu\text{m s}^{-1}$ (I), broad single line written with 0.24 wt.% Si444 at $v_{\text{IEX}} = 8.2 \mu\text{m s}^{-1}$ (II), split line written in 0.10 wt.% Si832 at $v_{\text{IEX}} = 12 \mu\text{m s}^{-1}$ (III), and a line in the region of inverted lines shown in panel (b), here written in 0.1 wt.% Si2.1 at very low $v_{\text{IEX}} \approx 0.2 \mu\text{m s}^{-1}$ (IV). Scale bars: 250 μm .

Additionally, for increasing velocities, the flux of incoming tracers is reduced and becomes too small for providing a large density contrast for the inverted line profile. Within all regimes, high diffusivities lead to a significant decrease in the line sharpness resulting again in lines unsuitable for actual writing. However, our model clearly predicts that single narrow lines of large density contrast are obtained for low diffusivity and intermediate IEX speed, exactly as observed in the experiments (c.f. the orange/yellow region in Figure 4b as compared to Figure 1b,c and Figure S1b-d, Supporting Information).

2.6. Graphical Application

Having explored the experimental and theoretical aspects of line writing in some detail, we turn to its graphical application. Here, we again use weakly charged tracers and moderate writing velocities, which is essential for proceeding beyond straight lines by combining line writing with steering. In the experiments, we controlled line orientation using a manually programmable, motorized stage, allowing sequences of changes in tilt direction and angle. In the BD simulations, we simply prescribed IEX speeds and trajectories. Figure 5 shows representative examples, in which we successfully produced some simple patterns and symbols (Figure 5a-f), drew complex patterns with multiple line crossings (Figure 5g), or wrote text (Figure 5h,i). Next, we discuss some practical issues encountered during their production. Downscaling is addressed for the example of a pattern with rectangular turns in Figure 5a-c. The right angles and straight intervals start washing out when the length of straights approaches three to two times the line thickness. Another issue is line-shifting. In the simulation run of Figure 5d, we compare the written line to the prescribed sinusoidal IEX trajectory. Due to the relatively long-ranged tracer attraction (Figure 3a) and the con-

tinuing DO-flows towards the back of the IEX (Figure 1g), the written line is dragged along in the overall propulsion direction. This results in a shift of the final line as compared to the prescribed IEX trajectory. The intended sinusoidal shape, however, is fully retained. This is different for the case of line crossing. For instance, in the simulation run of Figure 5e, the initial upward stroke of the lower-case Greek letter phi is bent to the left (see also Figure S18, Supporting Information). In addition, the freshly written line shows a local enhancement of line thickness (blob) also shifting in the propagation direction of the IEX. By contrast to blobbing by transient sticking of the IEX to the substrate (Figure S20, Supporting Information), blobbing upon line crossing is systematic. However, while it is kept at bay by high writing velocities ($v_{\text{IEX}} \geq 10 \mu\text{m s}^{-1}$), line bending is not. The inset of Figure 5e shows a line-crossing experiment at large v_{IEX} . Here, the duration of tracer attraction from the crossed high-density region is reduced, but the DO-flows are retained, and the line is still bent. In principle, line crossing can be avoided using multiple pens on merely touching trajectories (Figure 5f). Where it could not be avoided, we performed a stepwise adjustment of the stage tilting sequence to compensate for the observed and anticipated deviations from the desired line path (Figure S19, Supporting Information). With some experience, even complex patterns with multiple line crossings under desired angles, negligible line-bending, and little blobbing can be reproducibly drawn (Figure 5g). Note that the base of the “house” shown in Figure 5g is merely 500 μm and the height is about 850 μm , i.e., the house’s size is on the order of a single letter in this text. The figure was drawn within about five minutes at an IEX velocity of approximately $15 \mu\text{m s}^{-1}$. It retained its characteristic shape for more than 15 min. Writing of individual letters is less difficult. Picking up a certain tradition,^[9,10,12,14,15,20] we display the affiliation initials of the experimental and theoretical group in Figure 5h,i, respectively.

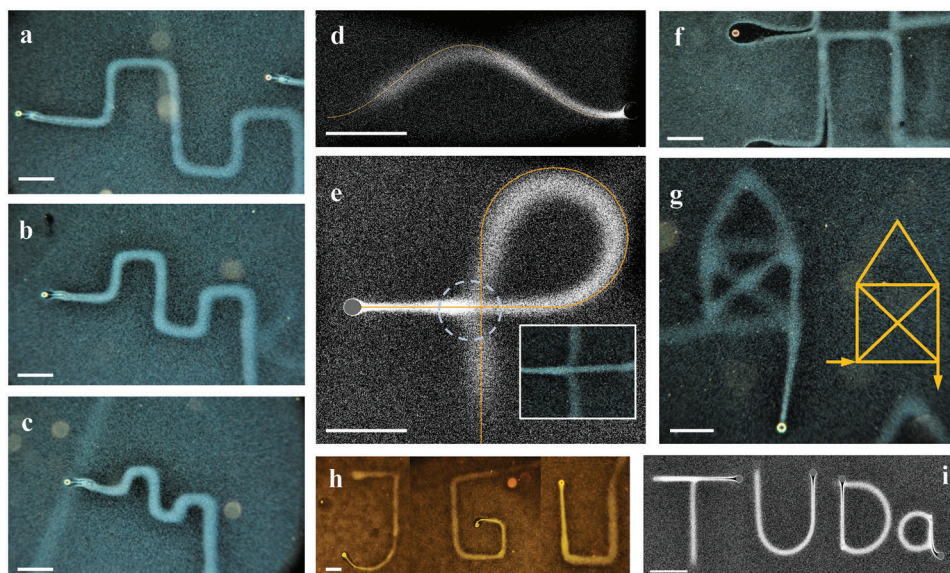


Figure 5. Examples of writing and drawing (experiments with C-IEX45 in Si832 and BD simulations with parameters as given in Table 2). All scale bars: 250 μm . a-c) Successive downscaling of pattern size. The length of the horizontals is 500 μm (a), 350 μm (b), and 175 μm (c). d) Sinusoidal line written in the BD simulation with parameters close to typical experimental ones (see Experimental Section, Table 2). Note the slight, leftward shift of the written line with respect to the IEX trajectory (solid yellow line). e) Lower case Greek letter phi with loop and line crossing. Note the bending of the crossed line and the formation of a region of enhanced density along the freshly written line (dashed circle). Inset: Writing at high IEX speed of $v_{\text{IEX}} = 10 \mu\text{m s}^{-1}$ reduces blobbing but retains line bending. f) Avoiding blob formation upon line crossing by mere line touching. g) One-line drawing of a complex pattern with rectangular and 45° angles as well as multiple line crossings. The inset shows the intended result (Das Haus vom Nikolaus). h) Initials of the Johannes Gutenberg University, Mainz, written with C-IEX45 in 0.2 wt.% Si832. i) Initials of the Technical University of Darmstadt written in a BD simulation with $v_{\text{IEX}} = 12 \mu\text{m s}^{-1}$.

2.7. Graphical Fine Tuning

So far, we concentrated on writing of and with durable, narrow lines of enhanced tracer density (positive contrast). This was facilitated by rolling C-IEX45 at speeds of $v_{\text{IEX}} = 6\text{--}10 \mu\text{m s}^{-1}$ through weakly charged Si832 ($\zeta_{\text{T}} = -68 \text{ mV}$) at 0.1-0.15 wt.% on native substrates ($\zeta_{\text{S}} = -105 \text{ mV}$). One may, however, wish to fine-tune the graphical appearance of the written lines. To this end, we exploit the modularity of our approach allowing tests of alternative inks, pens, and pen-drives. These additional and complementary experiments are described in detail in the Supporting Information (Figure S3-10). In short, tracers of larger or smaller size can be used to alter the line graininess and contrast. Replacing weakly charged tracers by highly charged tracers introduces additional diffusio-phoretic tracer motion. This alters the shape of the formation zone but leaves the decay zone unaffected (see also Movie S6, Supporting Information). The driving pH gradient can be manipulated by using different pen-types. Removing the pH gradient using chemically inert pens produces poor lines, while doubling the pH gradient using a pair of IEX yields thicker lines with weakly-charged tracers and split lines with highly-charged tracers. Replacing the anionic by a cationic IEX switches the sign of the pH gradient. Tracers are then repelled and the IEX curves a tracer free line into the background (negative contrast). Finally, we also tested different pen-driving mechanisms such as modular microswimmers self-assembling on horizontal substrates. These microswimmers propel autonomously and steer

by more or less random rearrangements of the assembled tracers. Lacking a directed steering, microswimmers write curved lines of otherwise good quality (see also Movie S7, Supporting Information).

3. Conclusion

The present approach of writing by assembly features several advantages over other approaches. As ink is available all along the trajectory, writing by assembly eliminates the necessity of a large (potentially eddy-creating) reservoir required in deposition-approaches as well as any re-filling issues. Working with small pens in a viscous fluid at low Reynolds numbers for the pen motion ($\text{Re}_{\text{pen}} \approx 10^{-4}\text{--}10^{-3}$) avoids eddy-creation, leaves the fluid practically undisturbed, and allows writing of narrow lines of a few tens of μm thickness, which compares favourably to the line widths reached in microprinting. With this approach, ink was collected from a region of a few pen diameters in width at Péclet numbers on the order of $\text{Pe}_{\text{ink}} \approx 5\text{--}50$. This was large enough for a quick build-up of significant density modulations. Chosen pen-speeds of $v_{\text{pen}} > 1.5 \mu\text{m s}^{-1}$ were large enough to avoid binding of the assembled micro-sized tracers to the pen and thus lead to line formation by tracer expulsion. At the same time, Pe_{ink} was small enough to avoid excessive direct transfer of kinetic energy to the ink particles. (This so-called dynamical friction may spoil the formation of highly visible lines, e.g., in the wake of a large star crossing a background of small stars in a globular cluster.^[45,46]) As a result, line dispersion occurred by diffusion only.

We demonstrated a facile and inexpensive approach to write on the micron scale within a liquid medium. A variety of further technical extensions awaits realization. Parallel writing of finely structured, large-scale density patterns becomes possible with several pens. Interruptions between words as well as dashed lines could be facilitated using photo-switchable chemical sources. Guided motion of the pen can further be realized by mechanical guiding,^[47] optical^[48] or magnetic forces,^[49] and chemical fields.^[50] Exploiting steering by chemical gradients would allow visualizing faint chemical traces left by other objects. Additionally, steering pH sources with optical tweezers in 3D buoyant ink dispersions would open access to freely suspended 3D patterns of arbitrary shape. Beyond global erasing by sonication, typo correction and line reconfiguration may be implemented by rewriting with or without prior heating with an IR laser (see also Movies S8 and S9, Supporting Information). Conversely, one could co-assemble suitable chemicals for line fixing like a mixture of photo-initiators, monomers, and cross-linker molecules. The important objective of further downscaling into the few- μm -range appears to be feasible for fluorescent tracers imaged by fluorescence microscopy and assembled by thermophoresis at a micron-sized heat source steered by laser tweezing. Adaptive learning and supervised machine learning could be used to program trajectories leading to the analog of handwriting. Already these few examples of possible future developments highlight an interesting point on the technical side: namely the versatility of our generic approach of combining ink assembly via long-ranged attractions with purely diffusive decay and programmable steering of the pen. It comprises a high degree of modularity, allows for the exchange of the constituents (pen, ink, drive) as to one's requirements, and is open for the combination with further modules. Thus, we anticipate that our results and conclusions are valid for a broad class of systems and may open routes to many future enterprises including the structuring of fluids, the visualization of chemical traces, the assembling of functional objects like actuators or drug carriers, information storage, and numerous artistic applications. Finally, our results could also be used to prepare desired initial states for future colloid experiments, e.g., on collective diffusion. Drawing fine lines, durable patterns, and individual letters into water was only the first step.

4. Experimental Section

Sample Preparation: As pens, micro-gel based cationic IEX beads (C-IEX45, Purolite Ltd, UK) are mainly used. The mean diameter ($2a = 45 \pm 2.3 \mu\text{m}$) was measured by image analysis. The IEX beads were recharged with H^+ ions by washing them twice in aqueous HCl (20 v/v%) solutions and subsequently rinsing them with deionized water. The beads were then stored for 48 h in an excicator. For some experiments, we also used anionic resin-based IEX beads or splinters thereof (A-IEX15, Mitsubishi Chemical Corporation, Japan and A-IEX-L, Carl Roth + Co. KG, Karlsruhe, Germany). These were only rinsed with deionized water and subsequently dried.

Passive ink particles were sulfate-stabilized polystyrene (PS) or silica (Si) colloidal suspensions (Microparticles, GmbH, Germany). **Table 1** denotes the lab codes, Manufacturer batch nos., sizes, and ζ -potentials where applicable. Prior to use, a part of the original stock (32 wt.%) was diluted with deionized water to 1 wt.% and conditioned for some weeks in a flask containing mixed-bed IEX (Amberjet, Carl Roth GmbH + Co. KG,

Table 1. Tracer colloids and IEX beads. Parameters of tracer colloids and IEX beads used in this work. ζ -potentials were determined from electrokinetic experiments using a custom-built Doppler Velocimeter.^[52]

Lab Code	Manufacturer Batch number	Diameter, $2a$ [μm]	ζ -potential under deionized conditions [mV]
Si444	SiO2-F-SC54	0.442 ± 0.054	-70 ± 3 (ambient CO_2)
Si832	SiO2-F-L1287	0.839 ± 0.031	-68 ± 3 (ambient CO_2) -108 ± 5 (de-carbonized)
Si2.1	SiO2-F-L4255-1	2.11 ± 0.18	N/A
PS2.3	PS/Q-F-L2090	2.30 ± 0.22	-35 ± 3 (ambient CO_2) -65 ± 5 (de-carbonized)
C-IEX45	CGC50 \times 8	45 ± 2	N/A
A-IEX-L	K306.2, Amberlite	250-400	N/A
A-IEX15	CA08S	$15.0 \pm 1,6$	N/A

Karlsruhe, Germany) to remove excess ions from the production process. After deionization, the IEX was removed, and the deionized suspensions stored in contact with ambient air. Thus conditioned, they show comparably low ζ -potential magnitudes due to CO_2 adsorption.^[51] CO_2 absorption can be reversed and any adsorbed CO_2 removed by further contact with mixed bed IEX in strictly gas-tight flasks.^[51] As compared to the merely deionized state, the deionized and de-carbonized state shows an approximately doubled ζ -potential magnitude.

The sample cell was constructed by sandwiching a chemically inert PVC ring (inner radius $R = 12.5 \text{ mm}$, height $H \sim 0.5 \text{ mm}$) between two standard microscopy slides ($75 \times 25 \times 1 \text{ mm}$, soda lime glass, hydrolytic class 3, VWR International, Germany). The ring was fixed to the bottom slide with epoxy glue (UHU plus sofortfest, UHU GmbH, Germany). Prior to cell assembly, the glass slides were thoroughly cleaned to remove coatings and organic contaminants (washing in 1 v/v% Hellmanex III-solution [Hellma Analytics, Germany], sonication in isopropanol for 30 min., rinsing with deionized water, and drying in N_2 flow). Right after cleaning, their ζ -potential was $\zeta = -138 \pm 8 \text{ mV}$. When stored in the dry state under ambient conditions, the ζ -potential magnitude decreased and equilibrated at $\zeta = -105 \pm 5 \text{ mV}$. The magnitude could be reduced further to $\zeta = -70 \pm 5 \text{ mV}$ by immersing the slides for one hour in diluted deconex cleaning solutions (5 v/v%, deconex 11, VWR, Germany).

Line Imaging: Cells were mounted on the stage of an inverted microscope (DMIRBE, Leica, Germany) and writing was observed at 10x magnification with a 12.87 Mpx. consumer DSLR (D700, Nikon, Japan) using a 0.63x mounting tube. In the images, 100 px correspond to $0.93 \mu\text{m}$. Images were captured in 14bit RAW format at intervals of 4s, converted to TIFF, and stored. Videos and cropped images for display were constructed from the TIFF color images. Data for further evaluation were converted to grey-scale and analyzed using a custom-written Python script. For $c \leq 0.2 \text{ wt.}\%$ of Si832, the recorded intensity was proportional to the tracer concentration, showing the absence of multiple scattering effects (Figure S2c, Supporting Information). Line profiles are constructed from intensity readings perpendicular to the line axes. For an individual profile, each $I(y)$ is an x-average over ten neighboring pixels. Typically, 50 individual profiles obtained from locations distributed over a distance of $\approx 100 \mu\text{m}$ along the written line were averaged to improve statistics. From fits of a Gaussian to the averaged profile, we extracted the line amplitude, standard deviation, and full width at half maximum.

Particle Image Velocimetry: For flow-field imaging, the stationary-state motion of tracers was studied using either the DSLR at 10x magnification and 200 fps or (for smaller tracers) a fast monochromatic camera (acA133-200um, Semi Python 1300, Basler, Germany) at 20x magnification and 100 fps. Flow fields were calculated from image pairs separated by $\Delta t = 100 \text{ ms}$ using the OpenPIV Python package. For each location, the results were averaged over 50 successive image pairs.

pH Microphotometry: For pH mapping, a further refined version^[42] of the general photometric approach reported by Niu et al. was employed.^[43] A diluted mixture of two universal indicators (pH 4–10, Merck, Germany; pH 1–5, Sigma–Aldrich, USA, ratio 1:7) was injected into the sample dispersion ($c = 100\text{--}200 \mu\text{mol L}^{-1}$). Images were recorded in transmission under Köhler illumination ($\langle \Delta I(x,y) / \langle I \rangle = 0.015$) using the DSLR camera. The 4.256×2.832 pixels on the CMOS-sensor are arranged in a Bayer pattern for the three RGB-channels resulting in dots of four px each, defining the maximum spatial resolution. For each dot, the recorded channel intensities were compared to those of a reference sample (deionized water) to obtain the absorbance in each channel from the Beer-Lambert–Law. Calibration was performed using pH buffer solutions ranging from pH 1.9 to 8.9 in 0.5 pH steps. For intermediate values, bicubic interpolation was used. The signal-to-noise ratio was improved by binning to 6×6 dots, reducing the final resolution to 357×237 blocks. At $10\times$ magnification, $5.8 \times 5.8 \mu\text{m}^2$ per block was observed. In the pH-range of interest (4 to 6), a height averaged pH-gradient resolution of 0.02 pH steps/ $6 \mu\text{m}$ resulted. Results were modeled by numerical solutions of the 3D advection–diffusion equation, which also yielded the pH-maps at specific locations, e.g., at the cell bottom.^[42]

Theoretical Model: The tracer particles were modeled as overdamped Brownian particles with radius a_T and were subject to an effective external force $\vec{F}_{\text{eff}}(t, \vec{r})$, which was centered around the IEX position and is explicitly time-dependent due to the IEX motion. The position of the i -th tracer particle evolved in time according to Equation (2). The effective (non-reciprocal) force $\vec{F}_{\text{eff}}(t, \vec{r})$ described the net impact of the IEX on the dynamics of the tracers. It is given as a sum of a short-ranged repulsion and a long-ranged attractive force \vec{F}_a [Equation (1)]. The former accounts for steric repulsion between tracers and IEX. The latter accounted for the net effect of the hydrodynamic flow that was created by the IEX. It was found empirically (Figure 3) that in the back of the IEX, the attractive force decays with the distance $\vec{R}(t) := \vec{r} - \vec{r}_{\text{IEX}}(t)$ from the IEX located at $\vec{r}_{\text{IEX}}(t)$ and moving deterministically at constant speed v_{IEX} as

$$\vec{F}_a(t, \vec{r}) = -\frac{\gamma_T c_1}{\left(|\vec{R}(t)|^\alpha + c_2 \right)} \frac{\vec{R}(t)}{|\vec{R}(t)|} \quad (3)$$

The constants c_1 and c_2 and the exponent α are determined from a fit to the velocity measurements (Figure 3 and Figure S11, Supporting Information). The uncertainties in c_1 and c_2 are rather large due to the interference of upward advection with lateral attraction for $|\vec{R}(t)| < 60 \mu\text{m}$. For simplicity, the asymmetry of the flow field was further neglected. Both were compensated by introducing an ad hoc factor 2 using $c_1 \approx 3.6 \times 10^4 \mu\text{m}^3 \text{s}^{-1}$. This resulted in a quantitative match of experimental observations and model predictions over an extended parameter range (Figure 4).

Brownian Dynamics Simulations: The equations of motion for the tracer particles were solved numerically in two spatial dimensions on an area $A = L_x L_y$ with periodic boundary conditions and area fraction $\varphi = N\pi a_T^2 / A$ by using LAMMPS.^[53,54] The repulsive part of the effective IEX–tracer interaction is modeled by a shifted Yukawa potential with strength $\epsilon_{\text{Yuk}} = 10k_B T_{\text{bath}}$, range $\sigma_{\text{Yuk}} = 1 \mu\text{m}$, and shift $\Delta r = a_{\text{IEX}}$.^[55] The time steps are $\Delta t = 10^{-4}$ s for non-interacting tracer particles and $\Delta t = 10^{-5}$ s for repulsively interacting tracer particles. All other simulation parameters are summarized in **Table 2**.

Continuum Theory: To describe the density distribution of the tracer particles in presence of the moving IEX, the Smoluchowski equation was formulated, which describes the time evolution of the probability density for finding a tracer particle at a point (t, X, Y) in space and time, where X and Y denote the coordinates in the laboratory frame.^[56] For simplicity, any direct tracer–tracer interactions were neglected here, i.e., $u(r) = 0$ in Equation (2). The continuum model only accounted for the net effect of the flow field and for the vol-

Table 2. Simulation parameters. Default parameters used for the BD simulations and the numerical solution of the continuum model if not stated explicitly.

Parameter:	Value:
a_{IEX}	22.5 μm
a_T	0.412 μm
γ_T	$7.854 \times 10^{-9} \text{ kg s}^{-1}$
v_{IEX}	8.0 $\mu\text{m s}^{-1}$
D	$0.5 \mu\text{m}^2 \text{ s}^{-1}$
φ	0.152
T_{bath}	298 K

ume exclusion between the IEX and the tracers using the total effective force

$$\vec{F}_{\text{eff}}(t, \vec{r}) = \vec{F}_a(t, \vec{r}) \tanh \left(\sqrt{(X - v_{\text{IEX}}t)^2 + Y^2 - a_{\text{IEX}}} \right) \quad (4)$$

with $\vec{r} = (X, Y)$ and IEX-radius a_{IEX} (see inset of Figure 3a). The IEX moves along the x -axis at a constant speed $v_{\text{IEX}} > 0$. We transformed the corresponding Smoluchowski equation for the probability density $p(t, X, Y)$ (we omit the arguments for clarity)

$$\frac{\partial p}{\partial t} = -\frac{1}{\gamma_T} \nabla \cdot (\vec{F}_{\text{eff}} p) + D \nabla^2 p \quad (5)$$

into the coordinate frame of the IEX by applying the Galilei transformation $x := X - v_{\text{IEX}}t$, $y := Y$. The transformed equation reads

$$\frac{\partial \tilde{p}}{\partial t} = -\frac{1}{\gamma_T} \nabla \cdot (\vec{F}_{\text{eff}} \tilde{p}) + v_{\text{IEX}} \frac{\partial \tilde{p}}{\partial x} + D \left(\frac{\partial^2 \tilde{p}}{\partial x^2} + \frac{\partial^2 \tilde{p}}{\partial y^2} \right) \quad (6)$$

where now $\tilde{p} = p(t, x, y)$. We omit the tilde throughout this work. Again, $D = k_B T_{\text{bath}} / \gamma_T$ denotes the tracer diffusion coefficient.

Numerical Solution Method: Equation (6) was solved numerically in two spatial dimensions on a rectangular area of size $(L_x, L_y) = (1000 \mu\text{m}, 200 \mu\text{m})$ with $x \in [-950 \mu\text{m}, 50 \mu\text{m}]$ and $y \in [-100 \mu\text{m}, 100 \mu\text{m}]$. The initial condition was given by a uniform distribution $p(0, x, y) = 1 / (L_x L_y)$. Dirichlet boundary conditions were used at the right, top, and bottom boundary with $p(t, 50 \mu\text{m}, y) = p(t, x, \pm 100 \mu\text{m}) = 1 / (L_x L_y)$ and no-flux boundary conditions at the left boundary, i.e., $\partial_x p(t, x, y)|_{x=-950 \mu\text{m}} = 0$. Finally, the Smoluchowski equation was solved with the NDSolve method from Mathematica^[57] by using the method of lines,^[58,59] finite element discretization,^[60] and the parameters displayed in Table 2.

Supporting Information

Supporting Information is available from the Wiley Online Library or from the author.

Acknowledgements

The authors thank A. P. Lanz for designing and realizing the programmable stage for writing, as well as D. Botin and P. Vogel for the characterization of tracers and substrate surfaces. This work was supported by the Max Planck Graduate Center with the Johannes Gutenberg-Universität Mainz (MPGC). Financial Support of the Deutsche Forschungsgemeinschaft (DFG) in the priority program SPP 1726 (Grant Nos. Pa 459/18-1 and Pa 459/18-2) is

gratefully acknowledged. N.M. is a fellow of the MPG. L.H. gratefully acknowledges the support by the German Academic Scholarship Foundation (Studienstiftung des deutschen Volkes).

Open access funding enabled and organized by Projekt DEAL.

Conflict of Interest

The authors declare no conflict of interest.

Author Contributions

N.M. and L.H. contributed equally to this work. N.M. and T.P. developed the concept of writing in water. N.M. built, performed, and evaluated the experiments. R.N. contributed to the single particle tracking experiments. L.H. and B.L. developed and performed the theoretical modeling. All authors contributed equally to data discussion and writing of the manuscript.

Data Availability Statement

The data that support the findings of this study are available from the corresponding author upon reasonable request.

Keywords

assembly, colloids, micron-scale, microswimmer, osmotic flow

Received: May 4, 2023
Revised: July 15, 2023
Published online: August 21, 2023

- [1] C. S. Henshilwood, F. d'Errico, K. L. van Niekerk, L. Dayet, A. Queffelec, L. Pollarolo, *Nature* **2018**, 562, 115.
- [2] S. D. Houston, *The First Writing: Script Invention as History and Process*, Cambridge University Press, Cambridge, **2004**.
- [3] F. d'Errico, C. B. Stringer, *Philos. Trans. R. Soc. B Biol. Sci.* **2011**, 366, 1060.
- [4] P. F. Bai, R. A. Hayes, M. Jin, L. Shui, Z. C. Yi, L. Wang, X. Zhang, G. Zhou, *Prog. Electromagn. Res.* **2014**, 147, 95.
- [5] T. H. Newman, K. E. Williams, R. F. W. Pease, *J. Vac. Sci. Technol. B Microelectron. Nanom. Struct.* **1987**, 5, 88.
- [6] A. Levskaya, A. A. Chevalier, J. J. Tabor, Z. B. Simpson, L. A. Lavery, M. Levy, E. A. Davidson, A. Scouras, A. D. Ellington, E. M. Marcotte, C. A. Voigt, *Nature* **2005**, 438, 441.
- [7] J. Li, E. H. Hill, L. Lin, Y. Zheng, *ACS Nano* **2019**, 13, 3783.
- [8] N. Vogel, M. Retsch, C.-A. Fustin, A. del Campo, U. Jonas, *Chem. Rev.* **2015**, 115, 6265.
- [9] S. Kim, B. Marelli, M. A. Brenckle, A. N. Mitropoulos, E.-S. Gil, K. Tsioris, H. Tao, D. L. Kaplan, F. G. Omenetto, *Nat. Nanotechnol.* **2014**, 9, 306.
- [10] M. Imboden, H. Han, T. Stark, E. Lowell, J. Chang, F. Pardo, C. Bolle, P. G. del Corro, D. J. Bishop, *Nanoscale* **2014**, 6, 5049.
- [11] *Nat. Nanotechnol.* **2016**, 11, 836.
- [12] A. Aubret, Q. Martinet, J. Palacci, *Nat. Commun.* **2021**, 12, 6398.
- [13] M. Eda, T. Yamasaki, M. Sakai, *J. Archaeol. Sci. Reports* **2019**, 26, 101875.
- [14] D. M. Eigler, E. K. Schweizer, *Nature* **1990**, 344, 524.
- [15] C. R. Moon, L. S. Mattos, B. K. Foster, G. Zeltzer, H. C. Manoharan, *Nat. Nanotechnol.* **2009**, 4, 167.
- [16] G.-Y. Liu, S. Xu, Y. Qian, *Acc. Chem. Res.* **2000**, 33, 457.
- [17] M. Liu, N. A. Amro, G. Liu, *Annu. Rev. Phys. Chem.* **2008**, 59, 367.
- [18] J. Im, Y. Liu, Q. Hu, G. F. Trindade, C. Parmenter, M. Fay, Y. He, D. J. Irvine, C. Tuck, R. D. Wildman, R. Hague, L. Turyanska, *Adv. Funct. Mater.* **2023**, 2211920.
- [19] J. Im, G. F. Trindade, T. T. Quach, A. Sohaib, F. Wang, J. Austin, L. Turyanska, C. J. Roberts, R. Wildman, R. Hague, C. Tuck, *ACS Appl. Nano Mater.* **2022**, 5, 6708.
- [20] Y. Guo, J. A. Belgodere, Y. Ma, J. P. Jung, B. Bharti, *Macromol. Rapid Commun.* **2019**, 40, 1900191.
- [21] R. S. Roberts, *Art Smith: Pioneer Aviator*, McFarland, Jefferson, North Carolina, and London, **2003**.
- [22] J. Anderson, *Annu. Rev. Fluid Mech.* **1989**, 21, 61.
- [23] J. L. Anderson, D. C. Prieve, *Sep. Purif. Methods* **1984**, 13, 67.
- [24] A. Würger, *Reports Prog. Phys.* **2010**, 73, 126601.
- [25] P. O. Staffeld, J. A. Quinn, *J. Colloid Interface Sci.* **1989**, 130, 69.
- [26] J. Palacci, C. Cottin-Bizonne, C. Ybert, L. Bocquet, *Soft Matter* **2012**, 8, 980.
- [27] A. Banerjee, H. Tan, T. M. Squires, *Phys. Rev. E: Stat. Phys., Plasmas, Fluids, Relat. Interdiscip. Top.* **2020**, 5, 073701.
- [28] A. Toyotama, T. Kanai, T. Sawada, J. Yamanaka, K. Ito, K. Kitamura, *Langmuir* **2005**, 21, 10268.
- [29] L. Lin, J. Zhang, X. Peng, Z. Wu, A. C. H. Coughlan, Z. Mao, M. A. Bevan, Y. Zheng, *Sci. Adv.* **2017**, 3, e1700458.
- [30] H. J. Keh, in *Encycl. Microfluid. Nanofluidics*, Springer US, Boston, MA, n.d., pp. 365–369.
- [31] S. Marbach, L. Bocquet, *Chem. Soc. Rev.* **2019**, 48, 3102.
- [32] R. Niu, P. Kreissl, A. T. Brown, G. Rempfer, D. Botin, C. Holm, T. Palberg, J. de Graaf, *Soft Matter* **2017**, 13, 1505.
- [33] R. Niu, T. Palberg, T. Speck, *Phys. Rev. Lett.* **2017**, 119, 028001.
- [34] M. Ibele, T. E. Mallouk, A. Sen, *Angew. Chemie* **2009**, 121, 3358.
- [35] R. Niu, E. C. Oğuz, H. Müller, A. Reinmüller, D. Botin, H. Löwen, T. Palberg, *Phys. Chem. Chem. Phys.* **2017**, 19, 3104.
- [36] M. J. Esplandiú, K. Zhang, J. Fraxedas, B. Sepulveda, D. Reguera, *Acc. Chem. Res.* **2018**, 51, 1921.
- [37] R. Niu, T. Palberg, *Soft Matter* **2018**, 14, 3435.
- [38] S. Michelin, E. Lauga, *Sci. Rep.* **2019**, 9, 10788.
- [39] A. Reinmüller, H. J. Schöpe, T. Palberg, *Langmuir* **2013**, 29, 1738.
- [40] R. Niu, D. Botin, J. Weber, A. Reinmüller, T. Palberg, *Langmuir* **2017**, 33, 3450.
- [41] A. Banerjee, T. M. Squires, *Sci. Adv.* **2019**, 5, eaax1893.
- [42] N. Möller, B. Liebchen, T. Palberg, *Eur. Phys. J. E* **2021**, 44, 41.
- [43] R. Niu, S. Khodorov, J. Weber, A. Reinmüller, T. Palberg, *New J. Phys.* **2017**, 19, 115014.
- [44] J. D. Weeks, D. Chandler, H. C. Andersen, *J. Chem. Phys.* **1971**, 54, 5237.
- [45] H. Aceves, M. Colosimo, *Am. J. Phys.* **2007**, 75, 139.
- [46] W. A. Mulder, *Astron. Astrophys. J.* **1983**, 117, 9.
- [47] J. Palacci, S. Sacanna, A. Vatchinsky, P. M. Chaikin, D. J. Pine, *J. Am. Chem. Soc.* **2013**, 135, 15978.
- [48] I. Buttinoni, G. Volpe, F. Kümmel, G. Volpe, C. Bechinger, *J. Phys. Condens. Matter* **2012**, 24, 284129.
- [49] A. Snezhko, M. Belkin, I. S. Aranson, W.-K. Kwok, *Phys. Rev. Lett.* **2009**, 102, 118103.
- [50] N. Möller, S. Seiffert, T. Palberg, R. Niu, *ChemNanoMat* **2021**, 7, 1145.
- [51] P. Vogel, N. Möller, M. N. Qaisrani, P. Bista, S. A. L. Weber, H.-J. Butt, B. Liebchen, M. Sulpizi, T. Palberg, *J. Am. Chem. Soc.* **2022**, 144, 21080.

- [52] D. Botin, J. Wenzl, R. Niu, T. Palberg, *Soft Matter* **2018**, *14*, 8191.
- [53] S. Plimpton, *J Comput Phys* **1995**, *117*, 1.
- [54] A. P. Thompson, H. M. Aktulga, R. Berger, D. S. Bolintineanu, W. M. Brown, P. S. Crozier, P. J. in 't Veld, A. Kohlmeyer, S. G. Moore, T. D. Nguyen, R. Shan, M. J. Stevens, J. Tranchida, C. Trott, S. J. Plimpton, *Comput. Phys. Commun.* **2022**, *271*, 108171.
- [55] H. Yukawa, S. Sakata, *Proc. Physico-Mathematical Soc. Japan. 3rd Ser.* **1937**, *19*, 1084.
- [56] H. Risken, *The Fokker-Planck Equation*, Springer, Berlin, Heidelberg, **1984**.
- [57] *Mathematica, Version 13.0*, Wolfram Research, Inc., Champaign, IL, **2021**.
- [58] S. Hamdi, W. Schiesser, G. Griffiths, *Scholarpedia* **2007**, *2*, 2859.
- [59] W. E. Schiesser, *The Numerical Method of Lines*, Academic Press, Inc., San Diego, **1991**.
- [60] G. Dhatt, G. Touzot, E. Lefrançois, *Finite Element Method*, ISTE, London, **2012**.